Anisotropic 4f-spin dynamics across the *B*–*T* phase diagram of Ce_7Ni_3

2006 J. Phys.: Condens. Matter 18 1955

(http://iopscience.iop.org/0953-8984/18/6/011)

INSTITUTE OF PHYSICS PUBLISHING JOURNAL OF PHYSICS: CONDENSED MATTER

J. Phys.: Condens. Matter **18** (2006) 1955–1966 doi:10.1088/0953-8984/18/6/011

Anisotropic 4f-spin dynamics across the B–T phase diagram of Ce_7Ni_3

A Schenck[1], F N Gygax[1], K Umeo[2], T Takabatake[2] and D Andreica[3]

[1] Institute for Particle Physics, ETH Zürich, CH-5232 Villigen PSI, Switzerland
[2] Department of Quantum Matter, Graduate School of Advanced Sciences of Matter, Hiroshima University, Higashi-Hiroshima 739-8530, Japan
[3] Babes-Bolyai University, Faculty of Physics, RO-3400 Cluj-Napoca, Romania

Received 30 August 2005, in final form 5 January 2006
Published 24 January 2006
Online at stacks.iop.org/JPhysCM/18/1955

Abstract

Longitudinal field μSR measurements in applied fields parallel and perpendicular to the c-axis of the hexagonal heavy-fermion antiferromagnet Ce_7Ni_3 served to monitor the 4f-spin dynamics across the magnetic phase diagram in the B–T plane, which consists of an incommensurate/commensurate antiferromagnetic (AF) section below 1.9 K/0.7 K and below an applied field B of 0.25 T, and for B along the c-axis, of a field-induced magnetic (FIM) section for $B \geqslant 0.6$ T and below 0.5 K. The observed μ^+ spin–lattice relaxation rates reveal persisting spin dynamics across the whole phase diagram, reflect the various phase boundaries and are interpreted to arise in the AF and FIM phases from the Ce3 sublattice (the Ce ions are located on three different sublattices) and in the intermediate phase, viewed as a short range ordered (SRO) state, also from the Ce1 and Ce2 sublattices with slower fluctuation rates. In the paramagnetic regime the Ce1 sublattice displays the slowest spin dynamics. In the FIM phase the fraction of relaxing μ^+ appears to shrink with rising B, evidencing a possible phase separation.

1. Introduction

The heavy-fermion compound Ce_7Ni_3 ($\gamma = 9$ J mol^{-1} K^{-2}) has received considerable attention because it is one of the few stoichiometric compounds which show non-Fermi-liquid behaviour near a quantum-critical point which can be reached by applying hydrostatic pressure of ∼0.4 GPa [1]. Under ambient pressure and below $T_{N_1} = 1.9$ K, Ce_7Ni_3 displays an incommensurate antiferromagnetic (iAF) order and below $T_{N_2} \simeq 0.7$ K part of the sample volume enters into a commensurate (cAF) order [2]. In the following we refer to these structures generally as the antiferromagnetic (AF) phase. The amplitude of the modulated ordered moment in the iAF phase is different for the three different crystallographic sites of Ce (see figure 1) and amounts to μ(Ce1) = 0.46 μ_B, μ(Ce2) = 0.7 μ_B and μ(Ce3) = 0.1 μ_B [2].

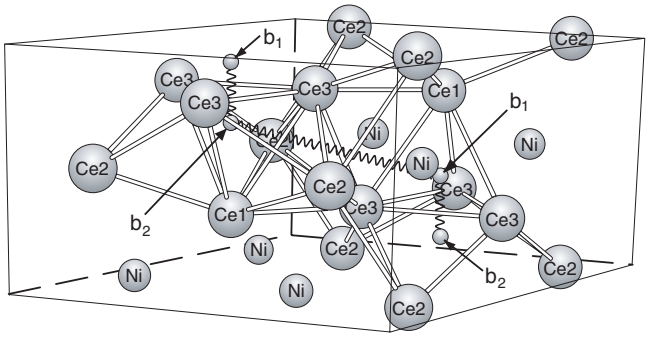

Figure 1. Hexagonal crystal structure (space group $P6_3mc$) of Ce_7Ni_3. The Ce ions are located at three different crystallographic sites: Ce1 is found at the *b*-site (2 per unit cell), Ce2 at a *c*-site (6 per unit cell) and Ce3 at another *c*-site (6 per unit cell). The μ^+ are found to reside at two different sites: $b_2 = \left(\frac{1}{3}\,\frac{2}{3}0.175\right)$ and $b_1 = \left(\frac{1}{3}\,\frac{2}{3}0.43\right)$ or, alternatively at $\left(\frac{1}{3}\,\frac{2}{3}0.405\right)$ and $\left(\frac{1}{3}\,\frac{2}{3}0.15\right)$ [5]. Below 3 K the majority of the implanted $\mu^+(\gtrsim 80\%)$ is located at the first site. The wavy lines represent suggested jump paths for μ^+ diffusion above 60 K [5].

More recent investigations show that not only is the phase diagram of Ce_7Ni_3 in the pressure–temperature plane of interest, but also the phase diagram in the field–temperature plane [3]. The latter studies show a rather complex phase diagram which is displayed in figure 2 and which looks rather different for different orientations of the external field $\boldsymbol{B}$ with respect to the crystal axes. For $\boldsymbol{B} \parallel c$-axis and $T < T_{N_1}$ the AF structure is destroyed in fields exceeding $\sim$0.25 T and a field-induced magnetic (FIM) phase seems to appear above $\sim$0.6 T and below the transition temperature ($T_M \lesssim 0.7$ K). Recently, a neutron diffraction study revealed that the magnetic unit cell in the *c*-plane for the FIM phase is three times that of the chemical unit cell [4]. For $\boldsymbol{B} \parallel c$-axis the $\left(\frac{1}{3}\,\frac{1}{3}0\right)$ magnetic reflection remains even in the field range $0.25\ \text{T} < B < 0.6$ T and temperature range $T < 1$ K. The magnetic state in this intermediate range is now viewed as a short range ordered (SRO) state. For $\boldsymbol{B} \parallel a$-axis T_{N_1} is almost unaffected by the strength of B up to at least 6 T and remains close to the zero field T_{N_1} ($\sim$2 K).

Studies of the electrical resistivity point to persisting spin fluctuations, perhaps along the *a*-axis, down to the lowest temperatures, involving the Ce3 spins, but the fluctuations may be largely quenched in the FIM phase [3]. This is thought to arise from a partial ordering of the Ce3 spins along the *c*-axis. The transition at T_M appears to be of first order [3]. The FIM phase is absent for $\boldsymbol{B} \parallel a$-axis.

It is argued that the behaviour of the Ce3 subsystem is caused by geometrical frustration, which prevents in zero field the full participation of the moments in the magnetic order below T_{N_1} and T_{N_2}, and explains even above T_M the small value of the ordered Ce3 moment [3].

In the present work we study the spin fluctuation scenario by muon spin–lattice relaxation rate measurements across the magnetic phase diagram for both $\boldsymbol{B} \parallel c$-axis and $\boldsymbol{B} \parallel a$-axis.

Previous transverse field (TF) μSR studies above 3 K have revealed that the implanted μ^+ occupy two different sites, namely two different tetrahedrally coordinated b-sites (see figure 1) [5]. The relative populations are strongly temperature dependent and one of the sites becomes very little populated close to T_{N_1} [5]. This has been confirmed by the TF μSR measurements below 2 K in the frame of this work. Muons showing a positive Knight shift (signal II) account for less than 20% of the implanted muons. Those showing a negative Knight shift (signal I) form the majority fraction [6]. The latter measurements below 2 K in fields up to 2 T appear to be consistent with a ferromagnetic alignment of the Ce3 spins along the *c*-axis

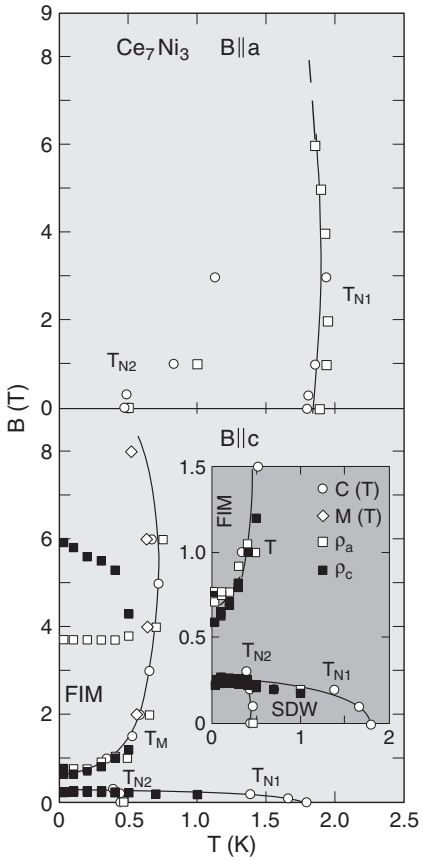

Figure 2. Magnetic phase diagram of Ce_7Ni_3 for $\boldsymbol{B} \parallel a$-axis (upper panel) and $\boldsymbol{B} \parallel c$-axis (lower panel) [3]. The field-induced magnetic phase is established above T_M. T_{N_1} refers to the incommensurate AF structure $[q_{ic} = (0, 0, \xi)]$ and T_{N_2} to the commensurate AF-structure $[q_c = (0, 0, \frac{1}{4})]$ which appears in part of the volume [2]. The various symbols refer to specific heat $[C(T)]$, magnetization $[M(T)]$ and resistivity $[\varrho_a, \varrho_c]$ measurements.

for $\boldsymbol{B} \parallel c$-axis starting, for example, at 40 mK at $B \simeq 0.35$ T [6], while the ferromagnetic alignment of the Ce1 and Ce2 moments is essentially complete at this temperature and field. In contrast for $\boldsymbol{B} \parallel a$-axis the absolute frequency shifts at 60 mK are proportional to the magnetization in the whole field range covered (0.05–2 T) with no indication for a change of the magnetic state, i.e., the AF phase seems to be preserved, in agreement with the phase diagram, figure 2, upper panel [7].

2. Experimental details

The measurements were performed at PSI using the low-temperature spectrometer LTF on the π M3 beam line. The single-crystal samples were flat plates covering approximately 1.0 cm^2. The c-axis, or the a-axis, respectively, was oriented perpendicular to the plate and parallel to the μ^+-beam axis and the applied field $\boldsymbol{B}$. The initial muon polarization $\boldsymbol{P}_\mu(0)$ was turned by ∼45°–50° by means of a spin rotator from horizontal towards the vertical direction. Hence it was possible to monitor simultaneously the time dependence of the component $P_\parallel(t)$ parallel

to $\boldsymbol{B}$ in forward and backward detectors and the precession signal $P_\perp(t)$ perpendicular to $\boldsymbol{B}$ in the left/right detectors of the LTF. The crystals were grown by the Czochralski pulling method starting from high purity (99.999%) material, and subsequently subjected to a further treatment to minimize defects, impurity atoms and strain [3]. The plates were cut by spark erosion from the ingots and carefully kept from exposure to air also during mounting of the sample into the dilution refrigerator of the LTF.

As is usual in a μ SR experiment, the evolution of the μ^+ polarization $\boldsymbol{P}(t)$ is monitored via the time-dependent decay asymmetry of the implanted spin-polarized ($\sim$100%) μ^+ by observing the positrons from the μ^+ decay in a certain direction $\boldsymbol{r}$ as a function of elapsed μ^+ lifetime. The positron rate can then be expressed as

$$\frac{\mathrm{d}^2 N_{\mathrm{e}^+}(t)}{\mathrm{d}t} = \frac{1}{4\pi\,\tau_\mu} N_0 \mathrm{e}^{-t/\tau_\mu}\,(1 - A\boldsymbol{P}(t)\cdot\boldsymbol{r})\,\mathrm{d}\Omega_r, \tag{1}$$

where A is the effective decay asymmetry (0.2–0.3), τ_μ the mean muon lifetime (2.2 μs), $|\boldsymbol{r}| = 1$ and $\mathrm{d}\Omega_r$ a solid angle element in the direction of $\boldsymbol{r}$. In the present case we consider only the signal obtained in the forward and backward counters, i.e., along the applied field $\boldsymbol{B}$, which leads to

$$\frac{\mathrm{d}^2 N_{\mathrm{e}^+}(t)}{\mathrm{d}t} = \frac{1}{4\pi\,\tau_\mu} N_0 \mathrm{e}^{-t/\tau_\mu}\,(1 - AP(t))\,\mathrm{d}\Omega_r, \tag{2}$$

with $P(t) \equiv P_\parallel(t)$ the depolarization function and $A = A_0\cos(\varphi)$, where A_0 is the total decay asymmetry and φ the angle by which $\boldsymbol{P}(0)$ was rotated up from the horizontal direction, i.e., from being parallel to $\boldsymbol{B}$. Note that A is only determined by the experimental arrangement, assuming that all implanted μ^+ contribute to $P(t)$. If one finds a reduced A a fraction of the implanted μ^+ either does not depolarize, i.e., $P(t) = 1$, or relaxes so quickly that $P(t) = 0$ within a few nanoseconds. In the following we will call A the signal amplitude.

3. Results

The measurements encompassed field scans at certain temperatures, exploring the phase diagram in figure 2 along vertical lines, and temperature scans along horizontal lines. Most generally $AP(t)$ was found to follow the two-component expression

$$AP(t) = A_\lambda \mathrm{e}^{-\lambda t} + A_\sigma \mathrm{e}^{-\frac{1}{2}\sigma^2 t^2}, \tag{3}$$

which is expected, if the μ^+ spins are exposed to static fields with a spread $\Delta B_i = \gamma_\mu \sigma$ ($\gamma_\mu = 2\pi\,1.355 \times 10^8$ rad T^{-1} is the gyromagnetic ratio of the μ^+) and to fluctuating fields $\tilde{B}_i$ causing the μ^+ spin polarization to relax with the rate λ, commonly known as spin–lattice relaxation. If the static fields are completely randomly oriented, as for example in powder samples, one expects in zero applied field $A_\lambda/A_\sigma = \frac{1}{2}$. In single crystals with non-random static fields, A_λ, for example, may vary between zero and the full initial asymmetry depending on the orientation of the initial μ^+ polarization with respect to the crystal axes. More precisely, the amplitudes A_λ and A_σ reflect the fractions of the initial μ^+ polarization, projected along the forward/backward direction or the applied field $\boldsymbol{B}$, affected by the fluctuating fields $\tilde{\boldsymbol{B}}_i$ and by the static internal fields $\boldsymbol{B}_i$, respectively. The sum $A_\lambda + A_\sigma$ may not necessarily be given by $A_0\cos\varphi$, as already pointed out in the previous section.

In principle all data are described by the four parameters λ, σ, A_λ and A_σ and, as we will find, all four parameters reflect the boundaries and sections of the magnetic phase diagram to various extents. In the following we first present the results of the various scans and will then list the salient features of the fitted parameters.

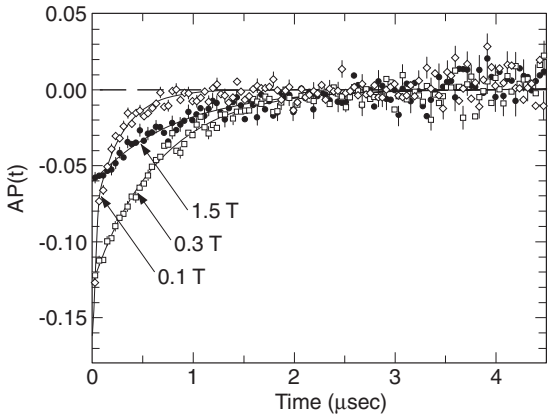

Figure 3. μSR signal at 40 mK obtained in the forward positron detector. The solid lines represent fits of equation (3) with $A_{\sigma_\parallel} = 0$ at 0.3 and 1.5 T.

3.1. Results of the field scans

For $\boldsymbol{B} \parallel c$-axis the field scans from 0.05 T up to 1.5 T were performed at 0.04 K, 0.2 K, 0.4 K (allowing us to cross into the FIM phase), and at 0.9 K (FIM phase absent) and at 2.5 K (paramagnetic phase only). Above 0.2 T only the exponentially damped term is seen. Some typical signals at 40 mK are shown in figure 3. The field dependences of the fitted $\lambda_\parallel$, $\sigma_\parallel$ and $A_{\lambda_\parallel}$ are displayed in figure 4.

For $\boldsymbol{B} \perp c$-axis the only field scan was performed at 60 mK. The two-component signal, equation (3), is observed up to 1 T. Fitted results for this orientation are displayed in figure 5.

3.2. Results of temperature scans

The temperature scans were performed at $B = 0.5$ T and 1 T for $\boldsymbol{B} \parallel c$-axis, and at $B = 1$ T for $\boldsymbol{B} \perp c$-axis, and hence yielded only a single exponentially damped component. The extracted temperature dependences of the relaxation rates $\lambda_\parallel$, $\lambda_\perp$ and asymmetries $A_{\lambda_\parallel}$, $A_{\lambda_\perp}$ are shown in figure 6.

The most important features displayed by the data are the following.

(i) The two-component behaviour for $\boldsymbol{B} \parallel c$-axis is restricted to the antiferromagnetic phases below T_{N_1} or T_{N_2}. The Gaussian relaxation rate $\sigma_\parallel$ reflects most likely the static internal field distribution $\boldsymbol{B}_i$ in the incommensurate antiferromagnetic phase. The sum $A_{\lambda_\parallel} + A_{\sigma_\parallel}$ appears constant and as $A_{\sigma_\parallel}$ decreases with rising B, $A_{\lambda_\parallel}$ increases by the same proportion. Above 0.2 T, $A_{\sigma_\parallel} = 0$ and the effective internal fields $\boldsymbol{B}_\mu = \boldsymbol{B} + \boldsymbol{B}_i$ must now be parallel to the forward–backward direction, i.e., parallel to $\boldsymbol{B}$, and the longitudinal μ^+ polarization component is only affected by fluctuating field components perpendicular to this component. Note that for $B \simeq 0$, in the AF phase $A_{\lambda_\parallel} \simeq 3\, A_{\sigma_\parallel}$. This implies that the internal fields are predominantly oriented along the c-axis. This is consistent with the c-axis orientation of the ordered moments in the AF phase.

(ii) The field dependence of the exponential relaxation rate $\lambda_\parallel$ for $\boldsymbol{B} \parallel c$-axis clearly reflects the phase boundary at $T_{N_1}(B)$ and is less pronounced at $T_M(B)$ in the temperature range 40 mK–0.4 K (see figure 4). At 0.9 K the FIM phase cannot be reached. Within the FIM phase $\lambda_\parallel$ becomes field independent or shows a slight tendency to increase and also rises with decreasing temperature. Also, at 0.9 K, $\lambda_\parallel$ is field independent above 0.3 T, but rises

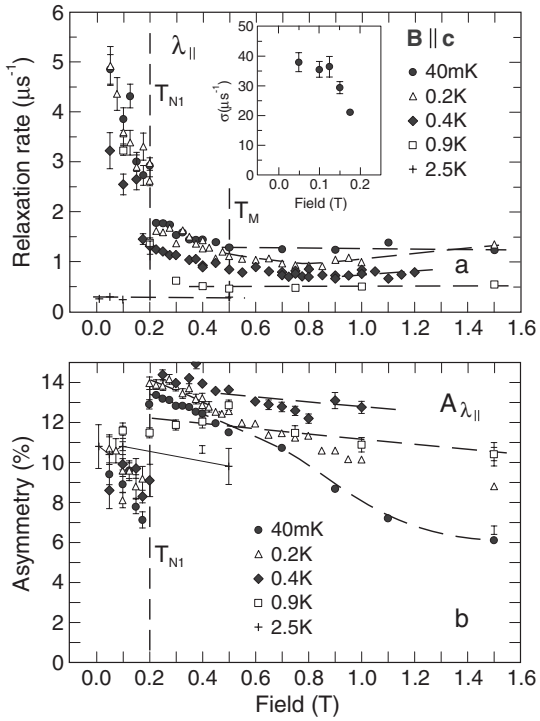

Figure 4. Field dependence of (a) $\lambda_\parallel$ and $\sigma_\parallel$ (inset) and (b) $A_{\lambda_\parallel}$ at various temperatures for $\boldsymbol{B} \parallel c$-axis. The dashed lines are intended to guide the eye. The vertical lines, labelled $T_{\mathrm{N_1}}$ and T_{M}, correspond to the critical fields at 40 mK at which the relevant phase boundaries are crossed.

when the antiferromagnetic phase is entered. At lower temperatures, $\lambda_\parallel$ exhibits a step-like singularity at the boundary to the AF phase. In the intermediate SRO phase, $\lambda_\parallel$ decreases weakly with rising B. Finally, at 2.5 K, above $T_{\mathrm{N_1}}$, $\lambda_\parallel$ is again field independent.

(iii) The weak field dependence of the asymmetry above the critical field of 0.2 T between 0.4 and 2.5 K (see figure 4, lower panel) is an instrumental effect which arises from the influence of the field on the positron and μ^+ trajectories. This leads to a change of the effective decay asymmetry. As can be seen from figure 4(b), the slope of $A_{\lambda_\parallel}(B)$ is the same at 0.4, 0.9 and 2.5 K. A rather different behaviour is seen at 40 mK and 0.2 K, i.e., inside the FIM phase. The asymmetry $A_{\lambda_\parallel}$ declines now much faster with rising B, most pronounced at the lowest temperature. This is also evident from figure 3, which shows directly the decrease of the signal amplitude when changing B from 0.3 to 1.5 T. This additional decrease on top of the instrumental effect seems to signal that the fraction of μ^+ being subject to depolarization shrinks as B is increased and the temperature decreased.

(iv) For $\boldsymbol{B} \perp c$-axis we find at 60 mK a rather different field dependence of the relaxation rates $\lambda_\perp$ and $\sigma_\perp$ and of the corresponding amplitudes $A_{\sigma_\perp}$ and $A_{\lambda_\perp}$. In accordance with the phase diagram no obvious anomalies are seen, since no phase boundaries are crossed. The persistence of the Gaussian damped component up to nearly 1 T is then not unexpected since the intrinsic fields $\boldsymbol{B}_i$ remain large and are not necessarily parallel to $\boldsymbol{B}$. Note also that $\sigma_\perp$ approaches values of $\sim$50 $\mu\mathrm{s}^{-1}$, corresponding to a field spread of $\Delta B_i = \sigma/\gamma_\mu \simeq 0.059$ T perpendicular to the applied field $\boldsymbol{B}$. The amplitude of the Gaussian component is proportional to $B_i^2/(B_i^2 + B^2)$, as expected [8] (solid line

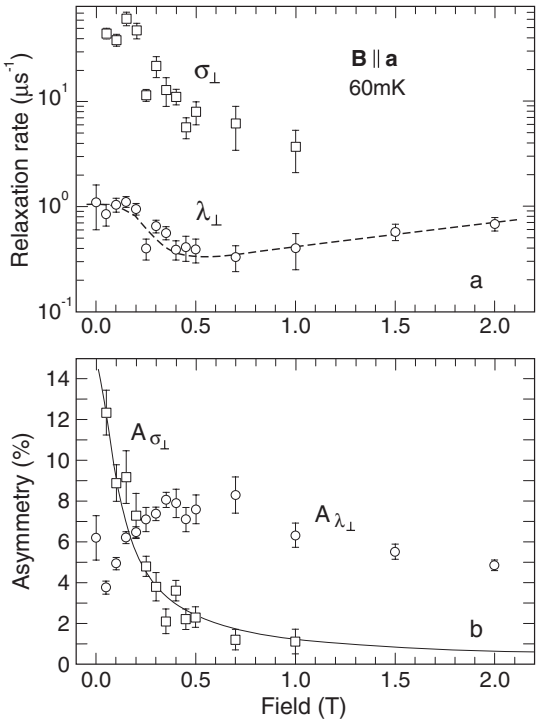

Figure 5. Field dependence of (a) $\lambda_\perp$, $\sigma_\perp$ and (b) $A_{\lambda_\perp}$, $A_{\sigma_\perp}$ for $\boldsymbol{B} \parallel a$-axis. The solid line in (b) is a fit as discussed in the text.

in figure 5(b)). The fit yields $B_i = 0.0825$ T, in qualitative agreement with the above estimated value. The exponential relaxation rate $\lambda_\perp$ is of the same magnitude as for $\boldsymbol{B} \parallel c$-axis. There is a significant strange dip in both $\sigma_\perp$ and $\lambda_\perp$ at 0.25 T, but not in $A_{\lambda_\perp}$ and $A_{\sigma_\perp}$, for which we have no explanation. In contrast to the case $\boldsymbol{B} \parallel c$-axis for $B \simeq 0$, we find $A_{\sigma_\perp} \simeq 3A_{\lambda_\perp}$. This is consistent with the previous conclusion that the static internal fields are predominantly oriented parallel to the c-axis.

(v) Looking at the results of the temperature scans, figure 6, we find significant temperature-dependent anisotropies of λ at $B = 1$ T. $\lambda_\parallel$ displays a clear change in temperature dependence at 0.6 K, which value falls nicely on the T_M curve (see figure 2). $A_{\lambda_\parallel}$ exhibits a clear cusp at the same temperature. In contrast, $\lambda_\perp$ displays a cusp at 1 K which coincides with some anomaly, seen in the resistance ϱ_a along the a-axis, and a change in slope of $\lambda_\perp(T)$ at $\sim$2 K which coincides with the crossing of the T_{N_1} line, i.e., the transition into the paramagnetic state. On the other hand, $A_{\lambda_\perp}$ appears temperature independent up to 0.8 K and then rises linearly with temperature up to 2 K, at which temperature a cusp-like behaviour appears. The latter anomaly reflects again the crossover into the paramagnetic regime, while the anomaly at 0.8 K agrees with an anomaly believed to reflect T_{N_2} (see figure 2). Note that any changes in the asymmetry A_λ can only reflect a change in the fraction of muons undergoing spin–lattice relaxation, since if all μ^+ would be subject to relaxation A_λ should be given by the initial longitudinal μ^+ polarization, which is a given instrumental quantity.

Interesting is also the behaviour of $\lambda_\parallel(T)$ and $A_{\lambda_\parallel}(T)$ at 0.5 T, which falls into the intermediate (SRO, paramagnetic?) region between the antiferromagnetic phase and the FIM

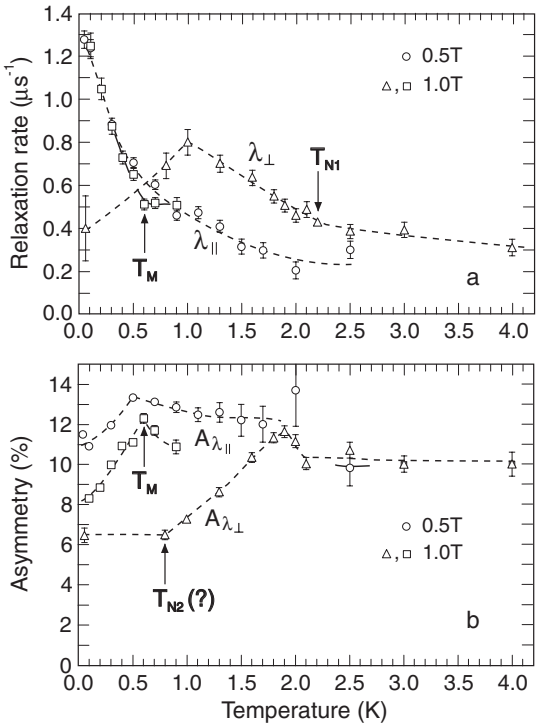

Figure 6. Temperature dependence of (a) $\lambda_\parallel$, $\lambda_\perp$ and (b) $A_{\lambda_\parallel}$, $A_{\lambda_\perp}$ at different fields. The dashed line are to guide the eye. The various relevant transition temperatures are indicated.

phase. As figure 6 shows, $\lambda_\parallel$ decreases smoothly with rising T and no anomalies show up. In contrast, $A_{\lambda_\parallel}$ displays an anomaly at 0.5 K, which temperature has no counterpart on the phase diagram. Further, a step-like change near 2 K may be visible, again without any corresponding point on the phase diagram. Note that at $B = 1$ T $\lambda_\perp < \lambda_\parallel$ for $T < 0.5$ K, and $\lambda_\perp > \lambda_\parallel$ for $T > 0.5$ K.

4. Discussion

The observed exponential relaxation of the implanted spin polarized muons implies the presence of temporally fluctuating fields of electronic origin at the μ^+ sites in all regions of the magnetic phase diagram in the (B, T) plane. As mentioned in the introduction, the μ^+ are located at two different sites with a population ratio of ∼5:1 below 3 K. The fact that only a single exponentially damped signal is observed outside of the AF phase suggests that the relaxation rates associated with the two different sites are of similar magnitude and that the fitted $\lambda_\parallel$ are dominated by the contribution from the most populated sites. Hence the estimates, following below, are based on the assumption that the μ^+ are located either at the site $\left(\frac{1}{3}\frac{2}{3}0.175\right)$ or, alternatively, at $\left(\frac{1}{3}\frac{2}{3}0.405\right)$; see the caption of figure 1. The field independence of $\lambda_\parallel$ at 40 mK in the FIM phase, assuming that $\lambda_\parallel$ follows the Redfield expression [9]

$$\lambda_\parallel = \gamma_\mu^2 \tilde{B}_i^2 \frac{\tau_c}{1 + \omega^2 \tau_c^2}, \tag{4}$$

implies that $\tau_c \omega \ll 1$, where τ_c is the correlation time or inverse fluctuation rate of the internal fields and $\omega = \gamma_\mu B$ the μ^+ Larmor frequency. Hence at $B = 1.5$ T, $\tau_c \ll \omega^{-1} \simeq 7.8 \times 10^{-10}$ s.

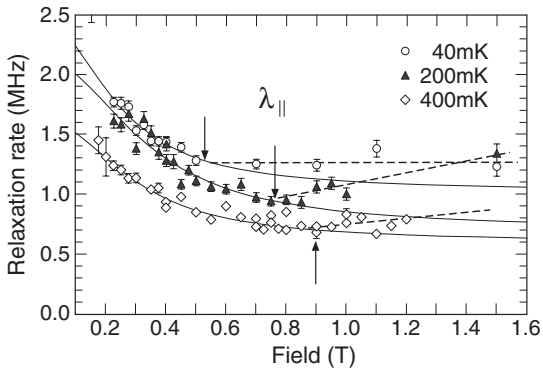

Figure 7. Field dependence of $\lambda_\parallel$ above the AF region. The solid lines represent fits of the modified equation (4), as described in the text, restricted to below the FIM phase. The dashed lines are guides to the eye in the FIM phase. The arrows denote the boundary to the FIM phase.

Table 1. Collection of fit results of the modified equation (4).

T (K)	τ_c (10^{-9} s)	$\gamma_\mu^2 \tilde{B}_{i,\parallel}^2$ (10^{14} s^{-2})	$\lambda_\parallel^0$ (μs^{-1})
0.04	4.72(1.87)	2.95(0.63)	1.025(0.147)
0.2	3.46(0.51)	4.05(0.40)	0.707(0.060)
0.4	3.93(0.81)	2.58(0.29)	0.597(0.050)
0.9	—	—	∼0.5[a]
2.5	—	—	∼0.3[a]

[a] From figure 4.

Equation (4) holds in the case that the Ce spin auto-correlation function decays exponentially with a mean decay time τ_c. This may not be necessarily true in the present case since the spin fluctuations in the ordered states may be (differently) correlated. Nevertheless, since equation (4) describes the field dependence of $\lambda_\parallel$ well, we use it empirically in the absence of a better model.

The weak field dependence of $\lambda_\parallel$ between T_{N_1} and T_M can be fitted by equation (4) with inclusion of a field-independent term $\lambda_\parallel^0$. The fit results are shown in figure 7 and table 1 for the data at 40, 200 and 400 mK. It is found that the fluctuating field amplitudes $\tilde{B}_i$ and τ_c at the different temperatures are equal within their error bars ($\tilde{B}_i \simeq 0.132$ T, $\tau_c \simeq 3 \times 10^{-9}$ s), while the main difference rests with the field-independent term $\lambda_\parallel^0$ (see table 1). The estimated $\tilde{B}_i$ are reasonable. Identifying $\tilde{B}_i^2$ with the second moment of the field distribution of randomly oriented moments on the Ce sites and considering only the majority sites, we calculate fluctuating fields $\tilde{B}_i$ from each Ce sublattice as listed in table 2. By comparison with fitted $\tilde{B}_i$, we estimate the fluctuating moments to amount to ∼0.13 μ_B if placed on the Ce1 sublattice, to ∼0.31 μ_B if placed on the Ce2 sublattice, and to 0.08 μ_B if placed on the Ce3 sublattice. This reasonable outcome may be taken as another justification for analysing $\lambda_\parallel(B)$ on the basis of equation (4). The field-independent term $\lambda_\parallel^0$ implies the additional presence of some much faster fluctuating fields, as already estimated above. With $\lambda_\parallel^0 = 1\ \mu s^{-1}$ and $\tau_c \ll 8 \times 10^{-10}$ s, we estimate that $\gamma_\mu^2 \tilde{B}_i^2 \gg 1.25 \times 10^{15}$ s^{-2} or $\tilde{B}_i \gg 0.26$ T, i.e., the fast fluctuating moment component may come close to the full Ce^{3+} paramagnetic moment.

Hence we are confronted with the peculiar situation that in the intermediate range between the antiferromagnetic phase and the FIM phase two different fluctuation rates associated with

Table 2. Calculated second moments $M_2^{ZF} = \tilde{B}_i^2$ with reference to the most populated μ^+ site.

		μ^+ site $(\frac{1}{3}\frac{2}{3}\ 0.175)$		μ^+ site $(\frac{1}{3}\frac{2}{3}\ 0.405)$	
Sublattice	$\boldsymbol{P}(0), \boldsymbol{c}$	M_2^{ZF} (10^{15} s^{-2} μ_B^{-2})	$\tilde{B}_i$ (T μ_B^{-1})	M_2^{ZF} (10^{15} s$^{-2}\mu_B^{-2}$)	$\tilde{B}_i$ (T μ_B^{-1})
Ce1	$\parallel$	7.19	0.625	7.43	0.636
	$\perp$	17.35	0.972	17.94	0.988
Ce2	$\parallel$	4.79	0.511	3.12	0.412
	$\perp$	3.89	0.460	2.86	0.395
Ce3	$\parallel$	56.05	1.747	63.85	1.864
	$\perp$	44.88	1.563	49.31	1.638

different sources coexist. At least up to 0.4 K the slower fluctuations appear to be temperature independent, while clearly the fast fluctuations are strongly temperature dependent. Since the fast fluctuations persist into the FIM phase it is reasonable to associate them with the Ce3 moments, while the slow fluctuations may arise from the Ce2 and Ce3 moments. On the other hand the temperature dependence of $\lambda_\parallel$ at 0.5 T, displayed in figure 6, must then reflect the temperature dependence of the fluctuation rate of the Ce3 moments, which behave paramagnetically down to and into the antiferromagnetic phase. The much stronger field dependence of $\lambda_\parallel$ in the antiferromagnetic phase implies reduced fluctuation rates of the paramagnetic Ce3 moments which, nevertheless, never approach a static behaviour.

As emphasized before, in the FIM phase only fast fluctuations are indicated, which may slow down a little bit as B is increased as indicated by a tendency of $\lambda_\parallel$ to rise with B. A similar rise is observed in $\lambda_\perp$ at 60 mK for $B > 0.5$ T (see figure 6), accompanied by a decrease of $A_{\lambda_\perp}$. Obviously a strong B can also, for this orientation, induce a slight slowing down of the Ce3 moment fluctuations.

Very interesting is the anisotropy of λ observed at 1 T (see figure 6(a)). At the lowest temperature $\lambda_\parallel/\lambda_\perp \simeq 3$, while above $\sim$0.7 K $\lambda_\parallel/\lambda_\perp < 1$. Since for $T \gtrsim 2$ K one is clearly in the paramagnetic regime, one could expect, on the basis of equation (4), that $\lambda_\parallel/\lambda_\perp \propto \tilde{B}_{i,\parallel}^2/\tilde{B}_{i,\perp}^2$. Consulting table 2, it is clear that the condition $\lambda_\parallel < \lambda_\perp$ can only be fulfilled if the fluctuating fields arise primarily from the Ce1 sublattice, which could imply that the correlation times τ_c are different for the different Ce sublattices with τ_c, associated with the Ce2 and Ce3 moments, too short to contribute to the μ^+ spin relaxation. The reversed anisotropy at the lowest temperature must be related to the fact that for $\boldsymbol{B} \parallel c$-axis one is in the FIM phase while for $\boldsymbol{B} \perp c$-axis one is in the antiferromagnetic phase, associated with different τ_c and, probably, $\tilde{B}_i$. Note also that $\lambda_\parallel > \lambda_\perp$ in the AF phase (compare figures 4(a) and 5(a)). This is consistent with the conjecture that the Ce3 spin fluctuations are directed perpendicular to the c-axis [3], i.e., $\tilde{B}_{i,\perp} > \tilde{B}_{i,\parallel}$, while for isotropic fluctuation $\tilde{B}_{i,\perp} < \tilde{B}_{i,\parallel}$ (see table 2).

Finally we comment on the field dependence of $A_{\lambda_\parallel}$ in the FIM phase. As emphasized before, the decrease of $A_{\lambda_\parallel}$ with increasing B implies that the fraction of μ^+ being subject to fluctuating fields must decrease with increasing B. This in turn implies that a certain separation of the sample volume into domains with fluctuating Ce3 spins and into domains without fluctuating Ce3 spins must evolve. This could indicate that in the latter domains the Ce3 spins participate in the field-induced magnetic order. It is not unreasonable to assume that the domains with paramagnetic Ce3 ions would completely disappear at much stronger fields. This view seems to be consistent with the interpretation of the electrical resistivity data which point to a quenching of the spin fluctuations in the FIM phase as mentioned in the introduction. The domains cannot be too small otherwise the separation of the μSR signal into a relaxing

and non-relaxing term would not be possible. In other words, a spatially random freezing of the Ce3 spins is not indicated. However, a two-phase behaviour is not only indicated in the field dependence of $A_{\lambda_\parallel}$ in the FIM phase but more generally also in the temperature dependence of $A_{\lambda_\parallel}$ as well as $A_{\lambda_\perp}$ outside of the AF phase (see figure 6(b)). According to our understanding this can only imply that the fractions of μ^+ being subject to spin–lattice relaxation depend on where in the magnetic phase diagram the μ^+ behaviour is monitored. This suggests that both in the SRO and FIM phase the fluctuating Ce 4f moments are confined to certain domains or volume fractions which depend on temperatures strength and orientation of the external fields with respect to the crystal axes. For $\boldsymbol{B} \parallel c$-axis the fraction of relaxing μ^+ clearly shrinks with decreasing temperature. The same is indicated for $\boldsymbol{B} \perp c$-axis when the T_{N_1} phase boundary is crossed to lower temperatures until possibly T_{N_2}. In summary, the relaxing μ^+ fraction, or the volume fraction of the fluctuating spin domains, respectively, become suppressed by low temperature and high magnetic fields. We attribute this behaviour to the Ce3 sublattice. The reason for the appearance of a kind of phase separation is not clear and needs further study also by other techniques.

5. Summary and conclusions

The results of our μSR measurements in longitudinal field geometry may be summarized as follows. At all fields and temperatures across the magnetic phase diagram of Ce_7Ni_3, spin–lattice relaxation of the implanted μ^+ is observed, implying spin fluctuations of some of the Ce ions involving one or more of the three distinct Ce sublattices. In the antiferromagnetic phase and the field-induced magnetic (FIM) phase the spin fluctuations are carried by the Ce3 sublattice. The fluctuations are fast and temperature dependent. The anisotropy of λ in the AF phase is consistent with the picture that the Ce3 spin fluctuations are restricted to a direction perpendicular to the c-axis, e.g. along the a-axis [2–4]. Particularly in the FIM phase, a fraction of the Ce3 ions, arranged in domains, ceases to exhibit spin fluctuations and appears to order ferromagnetically as well. This fraction grows with increasing applied field and decreasing temperature. In the range between the AF and FIM phase additional slower and temperature-independent fluctuating fields appear, which we associate with the Ce1 and Ce2 sublattices. The temperature independence could imply that the spin dynamics is dominated by exchange fluctuations unlike the temperature-activated spin fluctuations in the Ce3 sublattice. Evidently the Ce1 and Ce2 sublattices behave differently from the Ce3 sublattice also in the intermediate (SRO) regime. It is possible that the spin fluctuation in the Ce1 and Ce2 sublattices are ferromagnetically correlated. Finally, in the truly paramagnetic regime the Ce1 spins are the slowest fluctuating spins and induce the μ^+ spin relaxation, while the Ce2 and Ce3 spins seem to fluctuate much more quickly and do not contribute to the μ^+ spin relaxation.

The different spin dynamics associated with the different Ce sublattices may probably arise from the geometrical difference of the sublattices and related degree of frustration. Frustration is strongest for the Ce3 spins [3]. Not understood at this moment is the observation that the spins on the Ce3 sublattice apparently separate into different domains, particularly in the FIM phase.

Acknowledgments

This work has been performed at the Swiss Muon Source (SμS) of the Paul Scherrer Institut (PSI) and we are grateful to PSI and its Laboratory for Muon Spin Spectroscopy for providing excellent measuring conditions. The work was supported by the COE Research (13CE2002)

through a Grant-in-Aids from Ministry of Education, Culture, Sports, Science and Technology of Japan.

References

[1] Umeo K, Kadomatsu H and Takabatake T 1996 *Phys. Rev.* B **54** 1194
Umeo K, Kadomatsu H and Takabatake T 1996 *J. Phys.: Condens. Matter* **8** 9743
[2] Kadowaki H, Motoya K, Kawasaki T, Osakabe T, Okumura H, Kakurai K, Umeo K and Takabatake T 2000 *J. Phys. Soc. Japan* **69** 2269
[3] Umeo K, Echizen Y, Jung M H, Takabatake T, Sakakibara T, Terashima T, Terakura C, Pfleiderer C, Uhlarz M and v Löhneysen H 2003 *Phys. Rev.* B **67** 144408
[4] Umeo K, Motoya K, Kadowaki H, Aso N, Tayama T, Sakakibara T, Kurita N, Hedo M, Uwatoko Y, Takeuchi T and Takabatake T 2005 *J. Alloys Compounds* at press
[5] Schenck A, Andreica D, Gygax F N, Umeo K, Takabatake T, Schreier E, Kratzer A and Kalvius G M 2001 *J. Phys.: Condens. Matter* **13** 4277
[6] Schenck A, Gygax F N, Andreica D, Umeo K and Takabatake T 2003 *Physica* B **326** 394
[7] unpublished results
[8] see e.g. Schenck A, Gygax F N and Ōnuki Y 2003 *Phys. Rev.* B **68** 104422
[9] see e.g. Slichter C P 1978 *Principles of Magnetic Resonance* (Berlin: Springer)